photonics

MDPI

Article

Photonic Hook Initiated Using an Air–Liquid Interface

Liyang Yue [1,*], Bing Yan [1], Zengbo Wang [1], Oleg V. Minin [2] and Igor V. Minin [2,*]

[1] School of Computer Science and Electronic Engineering, Bangor University, Dean Street, Bangor, Gwynedd LL57 1UT, UK; b.yan@bangor.ac.uk (B.Y.); z.wang@bangor.ac.uk (Z.W.)
[2] School of Non-Destructive Testing, Tomsk Polytechnic University, 36 Lenin Avenue, Tomsk 634050, Russia; oleg.minin@ngs.ru
* Correspondence: l.yue@bangor.ac.uk (L.Y.); prof.minin@gmail.com (I.V.M.)

Abstract: In this paper, we demonstrate a novel photonic hook being initiated using an air–liquid interface (ALI). This bent light focus is produced by immersing a dielectric micro-cylinder partially at the edge of a thin liquid film whose thickness is smaller than the diameter of the micro-cylinder. Unlike the well-known properties of normal near-field focuses, this photonic hook propagates horizontally in the liquid along the ALI at specific depths and does not require the material processing of microscopic particles or the modulation of light irradiation for initiation. A morphological analysis indicates that the contrast in the refractive indexes of the ALI causes this phenomenon at the shadow end of the micro-cylinder with a transverse dimension smaller than the diffraction limit. Compared to previously discovered photonic hooks, the unique setup of this photonic hook can generate a force field that enables optical trapping in the region slightly beneath the ALI, and the related optical pressures have been simulated.

Keywords: photonic hook; optical force; mesotronics; Poynting vector; laser trap

Citation: Yue, L.; Yan, B.; Wang, Z.; Minin, O.V.; Minin, I.V. Photonic Hook Initiated Using an Air–Liquid Interface. *Photonics* **2023**, *10*, 1175. https://doi.org/10.3390/photonics10101175

Received: 8 September 2023
Revised: 3 October 2023
Accepted: 12 October 2023
Published: 23 October 2023

1. Introduction

A photonic jet is a near-field focusing phenomenon emerging from electromagnetic wave interaction with low-loss mesoscale dielectric objects on the shadow side, including micro/nanospheres, fibres, cubes, trapezoidal prisms, etc. [1–5]. It can deliver a strong field intensity enhancement over a relatively long distance of up to several wavelengths and possibly possesses a transverse dimension (beam waist) smaller than the diffraction limit [6]. These properties allow it to be used in applications such as detecting, imaging, and optical trapping [6]. Meanwhile, Minin et al. [7] discovered that the photonic jet does not propagate along a straight line under certain conditions and coined the term 'photonic hook' for the curved high-intensity light focus in this category [7–9]. It was the only example of artificial light bending apart from the Airy beam when it was invented [7,9]. Moreover, the radius of the curvature of a photonic hook is smaller than the wavelength of the illuminating light. This property is not presented in the family of Airy-like beams and is considered the smallest curvature radius of electromagnetic waves to date [9]. Serving as an example of an asymmetric optical phase shifting, a photonic hook is theoretically caused by the difference in the phase velocity and the interference of the wave produced by the contrast in the local refractive indexes inside or around the dielectric particles [7,9–11]. Initially, it was realised in the mean of a geometrical asymmetry, e.g., a wavelength-scaled dielectric cuboid combined with a wedge prism [7], and then developed to methods breaking the symmetries of the refractive indexes of the materials and illuminating light [9]. This adds a newfound degree of simplicity. According to this mechanism, Gu et al. used a Janus micro-cylinder made of two dielectric materials to produce the refractive index contrasts between the upper and lower halves of the cylinder, resulting in a photonic hook in the shadow direction of the micro-cylinder [12]. Minin et al. used partial illumination using a mask placed before the micro-cylinder to generate a similar half refraction for the initiation

of a photonic hook, rather than a double-material composition [13]. In addition, a photonic hook scalpel was designed based on this structure in 2021 [14].

The air–liquid interface (ALI) is the surface boundary between air and liquid. Its inhomogeneous nature can provide special physical/chemical environments to the micro/nano-objects compared with those in a single bulk phase because of the mechanism of mass transfer and the molecular orientation of the two phases [15], and an imbalance of intermolecular interactions and molecules in a higher energy state has been found at the ALI rather than in the liquid [16]. This creates applications such as the assimilation of molecular monolayers at the material surface (the Langmuir–Blodgett technique), ALI cell culture, etc. [17–19]. It is well known that photonic jets can improve optical trapping because of the regional enhancement of light intensity [3,20–26]. At the same time, the shape of the ALI and the refractive index distribution of the liquid film can negatively affect the generation of a normal, straight photonic jet. However, they can play a role in forming a photonic hook through the study reported in this paper.

In fact, we discovered a novel photonic hook initiated by and propagating along the ALI, based on the setup of a long dielectric micro-cylinder or an optical fibre core partially immersed at the edge of a thin water film. The original idea was offered by Minins and inspired by their publication [20]. The distributions of the $|E|^2$ field intensity and Poynting vector (power flow) are simulated to study its forming mechanisms by varying the thickness of the water film in this paper. Compared to the previous photonic hooks and normal optical trapping perpendicular to the ALI [22–26], the proposed photonic hook is oriented along and parallel to the ALI and is located in the area slightly beneath it, and thus may offer potential for optical trapping in that area in a transverse direction. This quality has not been discovered in photonic hooks before and is reported in this paper for the first time. Before transverse optical trapping was realised using laser tweezers equipped with engineered fibre tips to produce a local photonic jet [27,28], normally, a more sophisticated system needed to be added to trap nano-objects [29–31]. Equally, Yu et al. used a light field with a nonuniform spatial deformation to create multiple focal points for realising trapping in the longitudinal direction [32]. Brunetti et al. designed a dielectric nanobowtie dimer made up of two tip-to-tip silicon triangles to trap nanoparticles between the nanocavity [33]. Liang et al. investigated the optical trapping of multiple Rayleigh particles at different locations using four-petal Gaussian vortex beams [34]. However, all these recent results on optical trapping were achieved in a fully immersive environment and did not involve the effect on the ALI or the interface between the two media. Park and Furst built a model of optical trapping forces exerted using a single laser beam focused on a dielectric sphere located at a two-dimensional (2D) oil–water interface [35]. Li et al. developed an optical trapping system of fibre tips to transversely manipulate cells half-exposed in the air and half-immersed in the liquid [36]; nevertheless, it does not apply to work in a full-liquid environment inconsiderably beneath the ALI.. According to the aforementioned potential, the optical forces led by the proposed photonic hook are calculated for trapping a single particle when varying its position in the water film, and a capably curved force field is quantified in this process. Besides, solid material can be considered as a replacement for water in the model for the precise control of the film thickness in future experimental verification because of the complex micro-mechanics of liquid.

2. Modelling

Figure 1a illustrates a diagram of the proposed optical trapping system. A straight and long micro-cylinder is placed at the edge of a thin film of the liquid medium water to form the partial immersion, and the ALI separates the background medium—air and water in the shadow direction of the micro-cylinder, which is illuminated by a laser beam at a wavelength (λ) of 1064 nm [37] from the left side. The corresponding 2D numerical model is created based on the cross-section of the model in Figure 1a using the electromagnetic simulation software CST Studio Suite 2023 (CST), and the modelling diagram is shown in Figure 1b. The circular cross-section of a micro-cylinder (black profile in Figure 1b)

with a refractive index of n_1 = 1.6 and a diameter of 5 µm made of dense crown optical glass (SCHOTT N-SK4) [38] (high index at the wavelength of 1064 nm) is axially located in the x-axis direction, and has contact with a thin layer of water at the refractive index of n_2 = 1.33 [39] and a variable thickness. The background medium of the model is the air with a refractive index of n_0 = 1 (blue profile in Figure 1b). The open boundary condition is applied to simulate the large axial length of the micro-cylinder and the sufficient stretch of the liquid film in the $-z$ and $\pm x$ directions. The incident laser in the form of a plane wave is x-polarised and propagates along the z-axis in TE mode, shown as the red arrows in Figure 1b. Meanwhile, its electric field strength—$|E|$ is set to 1 V/m for all the models created by CST in this paper. Consequently, the $|E|^2$ field intensities shown in Figure 2 are considered the enhancements normalised to the intensity of the incident plane wave ($|E|^2 = 1$) in this case. Also, the corresponding magnetic field strength—$|H|$ is given by the equation of impedance of free space [40,41],

$$|H| = \frac{|E|}{Z_0} = \frac{1}{\sqrt{\frac{\mu_0}{\varepsilon_0}}} = \sqrt{\frac{\varepsilon_0}{\mu_0}} \cong \frac{1}{120\pi} \tag{1}$$

where Z_0, ε_0, and μ_0 are the impedance of free space, electric constant, and magnetic constant, respectively. The Poynting vector (power flow) is defined by the cross product [40,41],

$$S = E \times H \tag{2}$$

where S is the Poynting vector, E is the electric field (vector), and H is the magnetic field (vector). Based on Equations (1) and (2), the magnitude of the power flow of the incident plane wave is [40,41],

$$|S| = |E| \cdot |H| \cdot \sin 90^\circ \cong \frac{1}{120\pi} \tag{3}$$

Thus, all magnitudes of the power flows demonstrated in Figure 3 can be comparable to that for the incident light in order to quantify the related enhancement. All field distributions of this study are calculated by CST's frequency domain solver, which means that Maxwell's equations are transformed into the frequency domain, and every frequency sample would require solving an equation system in the model [42]. The theory of frequency sampling and its examples are provided in the CST help document [42].

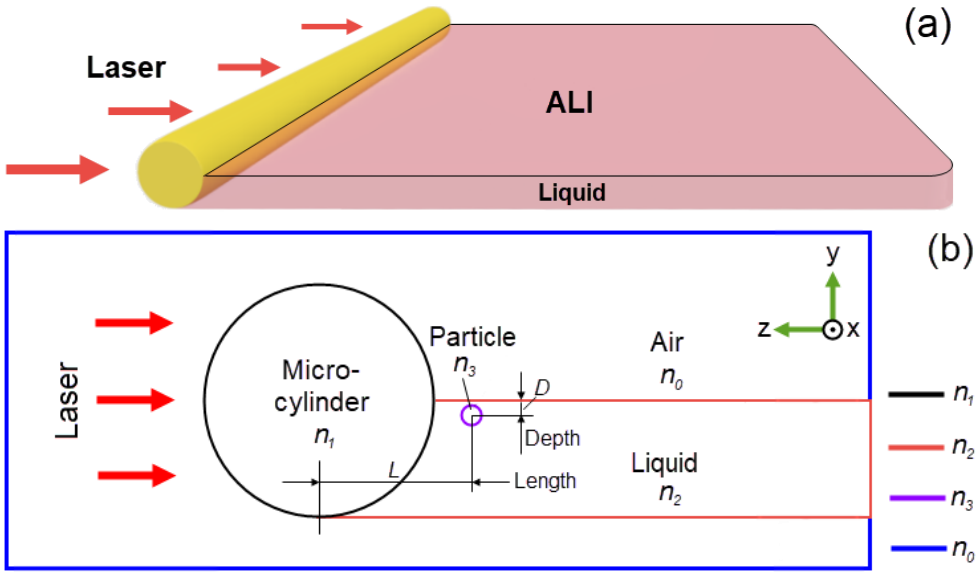

Figure 1. (**a**) Setup of a semi-immersive photonic hook and (**b**) CST modelling diagram.

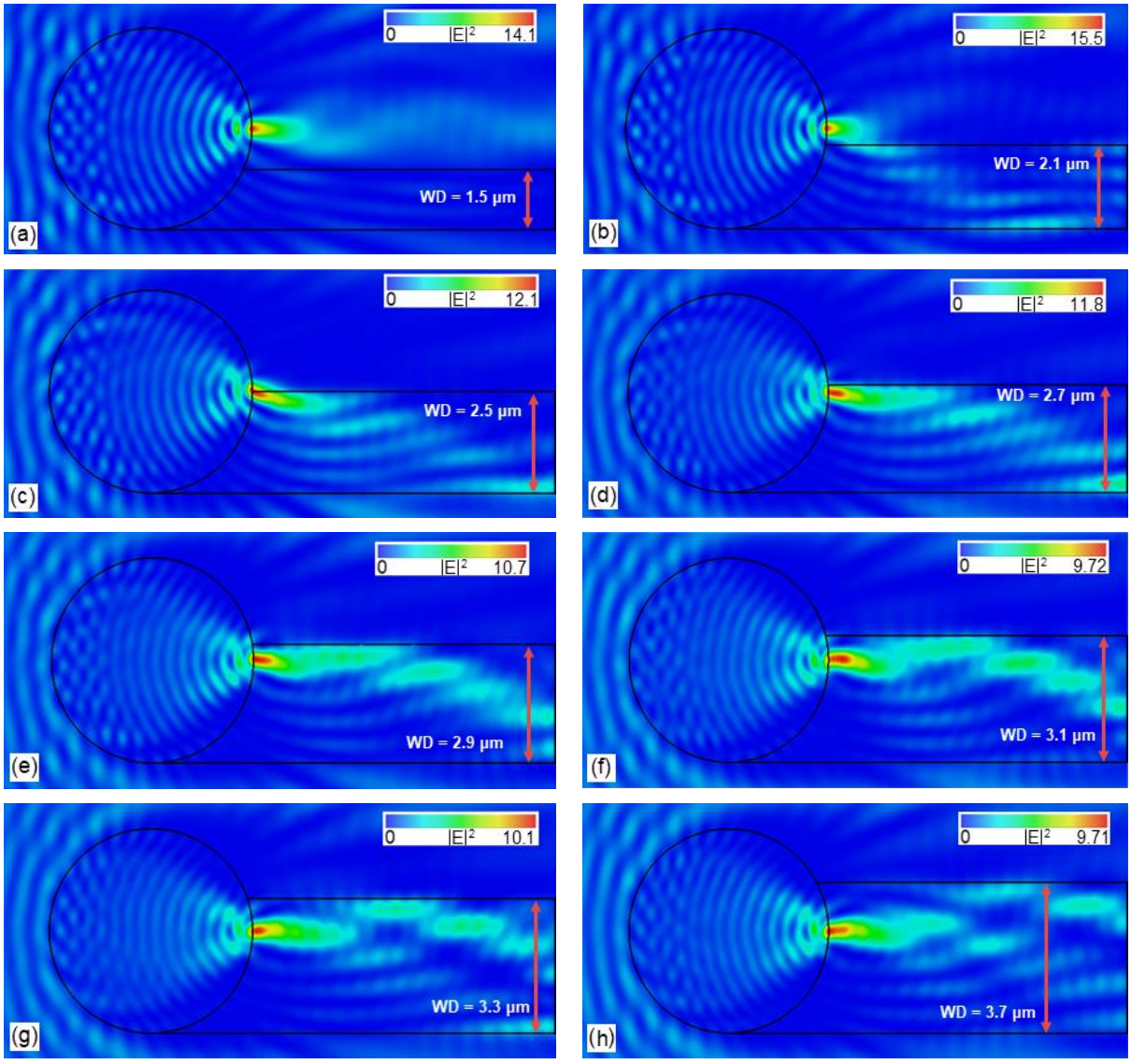

Figure 2. Intensities of $|E|^2$ fields for the models with multiple thicknesses of water layers—(**a**) 1.5 μm, (**b**) 2.1 μm, (**c**) 2.5 μm, (**d**) 2.7 μm, (**e**) 2.9 μm, (**f**) 3.1 μm, (**g**) 3.3 μm, and (**h**) 3.7 μm.

A simplified mechanical model of optical force is built based on the propagation (+z to −z) and polarisation (TE mode) of the incident plane wave using a MATLAB programme. The 2D transverse (F_y) and axial (F_z) optical pressure (unit: N/m) to the trapping target are given by [43],

$$F_y = \frac{1}{2}\oint_{S_1}\left\{\frac{1}{2}\left[\mu\mu_0|H_y|^2 - \varepsilon_0\varepsilon_1|E_x|^2 - \mu\mu_0|H_z|^2\right]d_z + \mu\mu_0 Re\left(H_y H_z^*\right)dy\right\} \quad (4)$$

$$F_z = \frac{1}{2}\oint_{S_1}\left\{\frac{1}{2}\left[\mu\mu_0|H_z|^2 - \varepsilon_0\varepsilon_1|E_x|^2 - \mu\mu_0|H_y|^2\right]d_y + \mu\mu_0 Re\left(H_z H_y^*\right)dz\right\} \quad (5)$$

Here, S_1 is a contour that envelops the object cross-section on the yz-plane. E_x, H_y, and H_z are the electromagnetic field components in the x, y, and z directions. ε_0 and ε_1 are the permittivity of the vacuum and medium, respectively. μ is the permeability of the medium, and μ_0 is the permeability of the vacuum. Furthermore, the position of the polystyrene micro-cylindrical particle (PS particle, refractive index, n_3 = 1.57 [44]; diameter, 100 nm), which serves as the trapping target fully immersed in the water film, is represented by two variables, D and L—the depth to the ALI and the distance to the micro-cylinder

centre. It is noted that the force field in this mechanical model is achieved using normalised distributions of the electric and magnetic field strengths from an incident plane wave, as introduced above, with the magnitude of the electric field set to 1 V/m. This means that the optical force pressures induced by the proposed photonic hook can increase by several orders of magnitude through the enhancement of the incident light intensity. Due to this and the fact that the PS particle is fully immersed, the effects of surface tension, capillary forces, Van der Waals forces, thermal stochastic forces, and Brownian motion are ignored for simplicity, without reducing the generality of the problem.

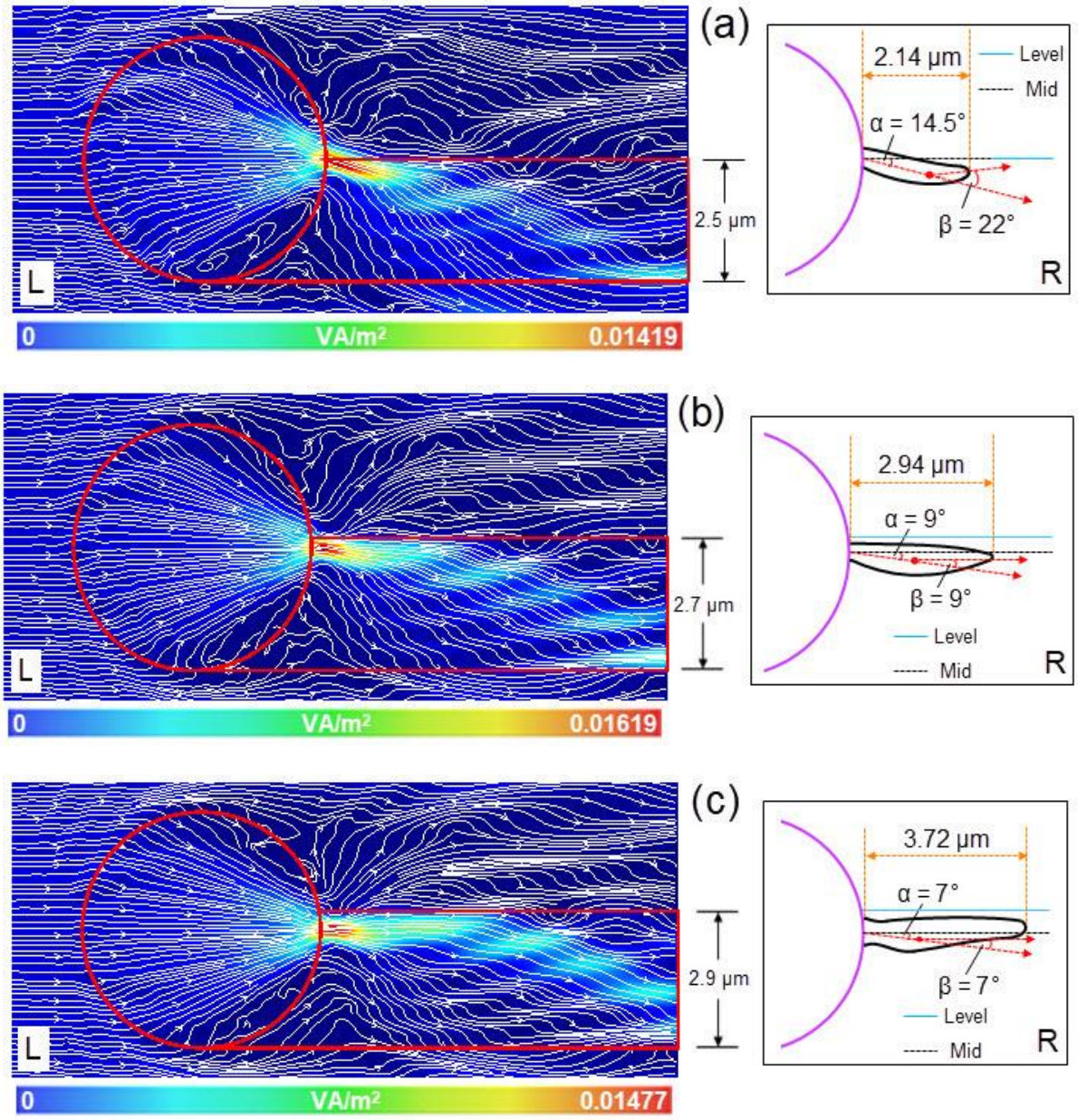

Figure 3. Magnitudes and flows of the Poynting vector for models with water films of (**a**) 2.5 μm, (**b**) 2.7 μm, and (**c**) 2.9 μm thicknesses.

3. Results and Discussion

3.1. Electric Field Intensities

Figure 2a–h demonstrate the intensities of the $|E|^2$ fields for the models paired with multiple thicknesses of water layers. The thickness of the water film plays a major role in changing the shape, length, and position of the near-field focus of the micro-cylinder.

In Figure 2a,b, the micro-cylinders are immersed in water films whose thicknesses are smaller than their radii, and the corresponding focuses are straight, small, and narrow high-field-intensity areas, which are the typical features of a photonic jet. However, this tendency tends to convert to photonic hooks when the thickness of the water film is larger than the radius of the micro-cylinder, which is 2.5 μm. For this reason, the near-field focuses shown in Figure 2c–f are considered photonic hooks, which are towards the bottom at the beginning and then inflect to the ALI with curvatures in the middle. The total internal reflection effect appears to confine the lights to the water film near the interface in these cases. By contrast, the focuses in Figure 2g,h are relatively straight compared to those in Figure 2c–f, despite a slight bending. Therefore, the photonic hooks shown in Figure 2c–f are different from the photonic hooks discovered before [7,9,11], which were caused by the contrast in refractive indexes at the incident end of the Janus particle where the light enters [7]. In this case, the light encounters corresponding contrasts in the refractive indexes at the boundaries separated by the ALI (from glass to air in the upper half; from glass to water in the lower half) at the shadow end after propagation through the entire dielectric micro-cylinder. When the incident light propagates along the ALI, its wavefront travels in two media—the upper part in the air and the bottom part in the water, which results in the difference in phase velocity to bend the focus for forming a photonic hook. It is indicated that the gradient of the refractive index can drive the deflection of the photonic hooks at the appropriate depths to advance the ALI and further elongate them, which results in the morphological differences shown in Figure 3. Meanwhile, changing the liquid material may provide another degree of freedom to bend the photonic hook.

Also, the diffraction limit (DL) is a fundamental constraint on the resolution of the optical systems determined by the wavelength of light and the numerical aperture of the optical systems according to the Rayleigh criterion [45]. The full widths at half maximum (FWHM) refers to the width of the intensity distribution at half of its maximum intensity. In the context of imaging resolution and the diffraction limit, this parameter is crucial as it defines the spatial extent of the focused light [45]. If the FWHM of a near-field focus is smaller than the DL, the features smaller than the DL can be resolved as separate entities under it in principle. Table 1 summarises the FWHMs of the photonic hooks shown in Figure 1, along with a comparison to the DLs in the corresponding media, which were calculated using the expression of $\lambda/2n$. It should be noted that the FWHMs of the photonic hooks in this paper are shorter than the DLs regardless of which media the hotspots (the positions of maximum field intensity) are located in. The results in Table 1 show that the photonic hook with a thickness of 2.1 μm (in Figure 2b) provides the largest percentage decrease of 40.23% compared to DL. Meanwhile, the hotspot of the photonic hook with a thickness of 2.5 μm (in Figure 2c) is at the ALI and covers two media—air and water. As a result, there are two DLs in the third row of Table 1 corresponding to air and water. The photonic hook with a thickness of 2.7 μm has the shortest FWHM, with a length of 0.310 μm and a percentage decrease of 22.50% compared to the DL of water. It is noted that the photonic hooks initiated by the ALI can possess FWHMs that are smaller than the DLs. Equally, a curved light beam, such as a photonic hook, can yield a larger field of view for near-field imaging with higher contrast and resolution because of its asymmetric excitation pattern [46]. Therefore, these characteristics would be meaningful for building a trapping/nano-imaging 2-in-1 optical setup.

Table 1. Comparison between FWHMs of the photonic hooks and DLs.

Thickness (μm)	FWHMs (μm)	DLs (μm)	Percentage Decrease
1.5	0.360	0.532–$\lambda/2n_0$	−32.33%
2.1	0.318	0.532–$\lambda/2n_0$	−40.23%
2.5	0.369	0.532–$\lambda/2n_0$	−30.64%
		0.400–$\lambda/2n_2$	−7.75%

Table 1. *Cont.*

Thickness (μm)	FWHMs (μm)	DLs (μm)	Percentage Decrease
2.7	0.310	$0.400–\lambda/2n_2$	−22.50%
2.9	0.343	$0.400–\lambda/2n_2$	−14.25%
3.1	0.366	$0.400–\lambda/2n_2$	−8.50%
3.3	0.359	$0.400–\lambda/2n_2$	−10.25%
3.7	0.362	$0.400–\lambda/2n_2$	−9.50%

Note: n_0 and n_2 represent the refractive indexes of air and water, respectively.

3.2. Poynting Vector Flows

The left column of Figure 3 (marked L) illustrates the magnitudes and flows of the Poynting vector for the photonic hooks generated in water films with thicknesses of 2.5 μm, 2.7 μm, and 2.9 μm, respectively. These are comparable to the $|E^2|$ fields shown in Figure 2c–e. The right column (marked R) shows the profiles of these three photonic hooks (contour of the exponential decay of the maximum magnitudes of the Poynting vector to 1/e), including their lengths and positions relative to the water level and middle axis in the shadow part of the micro-cylinder. The curvatures of the photonic hooks are represented by two parameters—angle α and angle β, which denote the bend angles for the beginning of the photonic hook to the middle axis and its end part to the beginning, respectively. The thicknesses of the three water films in Figure 3 are all relatively close to the radius of the micro-cylinder. This means that the distance between the water level and the middle axis plays a role in the development of the photonic hook in this mechanism. It is found that the contrasts in the refractive indexes exist at the boundaries between the micro-cylinder and media of air and water in the shadow regions above and below the ALI, respectively. This leads to asymmetric focusing around the area that is close to the middle axis in the shadow part of the model. In Figure 3 Ls, the corresponding inflections of the Poynting vector streamlines through the micro-cylinder boundary above the ALI are larger than those below the ALI at the flanks due to a larger contrast in the refractive indexes (glass/air—n_1/n_0 = 1.6 > glass/water—$n_1/n_2 \approx 1.2$). This results in two asymmetrically triangular areas with low magnitudes of the Poynting vectors on both sides of the focus waist, which further reduces its size longitudinally. Moreover, the Poynting vector flows with larger inflection in the upper triangle over the ALI can guide the near-field focus downwards during propagation to form the proposed photonic hook.

Furthermore, the ALI creates a contrast in the refractive indexes between the water and air, causing the Poynting vector flows to be transversely separated. This is reflected in the regular oscillation of the streamlines, which appears as a rebound effect at the ALI in both media simultaneously, as shown in Figure 3a–c Ls. This wavy tendency elongates the photonic hook and is particularly pronounced near its end, gradually diminishing as it moves deeper into the water film. The statistics of three photonic hooks are presented in Figure 3a–c Rs, where it is observed that the lengths and curvatures of the photonic hooks are inversely proportional. Especially, the shortest photonic hook in Figure 3a has the largest α and β angles, whereas the longest photonic hook and smallest α and β are both shown in Figure 3c. The larger angle α of the photonic hook in Figure 3a is due to the presence of an optical vortex near the shadow surface of the particle [18,47]. Based on the aforementioned theory, both the asymmetrically longitudinal guidance of the refractive index contrast and the transverse oscillation along the ALI contribute to the formation mechanism of the proposed photonic hook, with their individual effects being controlled by the thickness of the water film. In a model with a relatively thinner water film, such as Figure 3a, the photonic hook is primarily guided by the longitudinal effect and exhibits more pronounced bending. Conversely, the transverse oscillation along the ALI plays a greater role in the model with a thicker water film, as seen in Figure 3c, resulting in a longer photonic hook.

3.3. Optical Forces

Figure 4 illustrates the 2D transverse and axial optical force pressures—F_x and F_z exerted on the PS particle at various depths—D and distances from the micro-cylinder centre—L for the water films of thicknesses (a) 2.5 µm and (b) 2.9 µm. To collect data on the calculated optical forces, the PS particle was horizontally positioned at specific depths with a step width of 50 nm, ranging from L = 2650 nm to L = 6550 nm, taking into account the radius of the micro-cylinder (2500 nm) and diameter of the PS particle (100 nm). As a result, a large amount of data was generated, and only representative examples are shown in Figure 4 for depths of D = 80 nm, 130 nm, 250 nm, 400 nm, 500 nm, 700 nm, and 1000 nm. The relative positions of the data points with respect to the generated photonic hooks are depicted in the insets of Figure 4a,b, corresponding to the shaded areas (photonic hook—PH length) in the main graphs. The indicators of force direction (solid black lines) are located at the 0 positions in Figure 4, showing that forces greater than 0 are in the $+y$ and $+z$ directions, with the opposite direction corresponding to negative values.

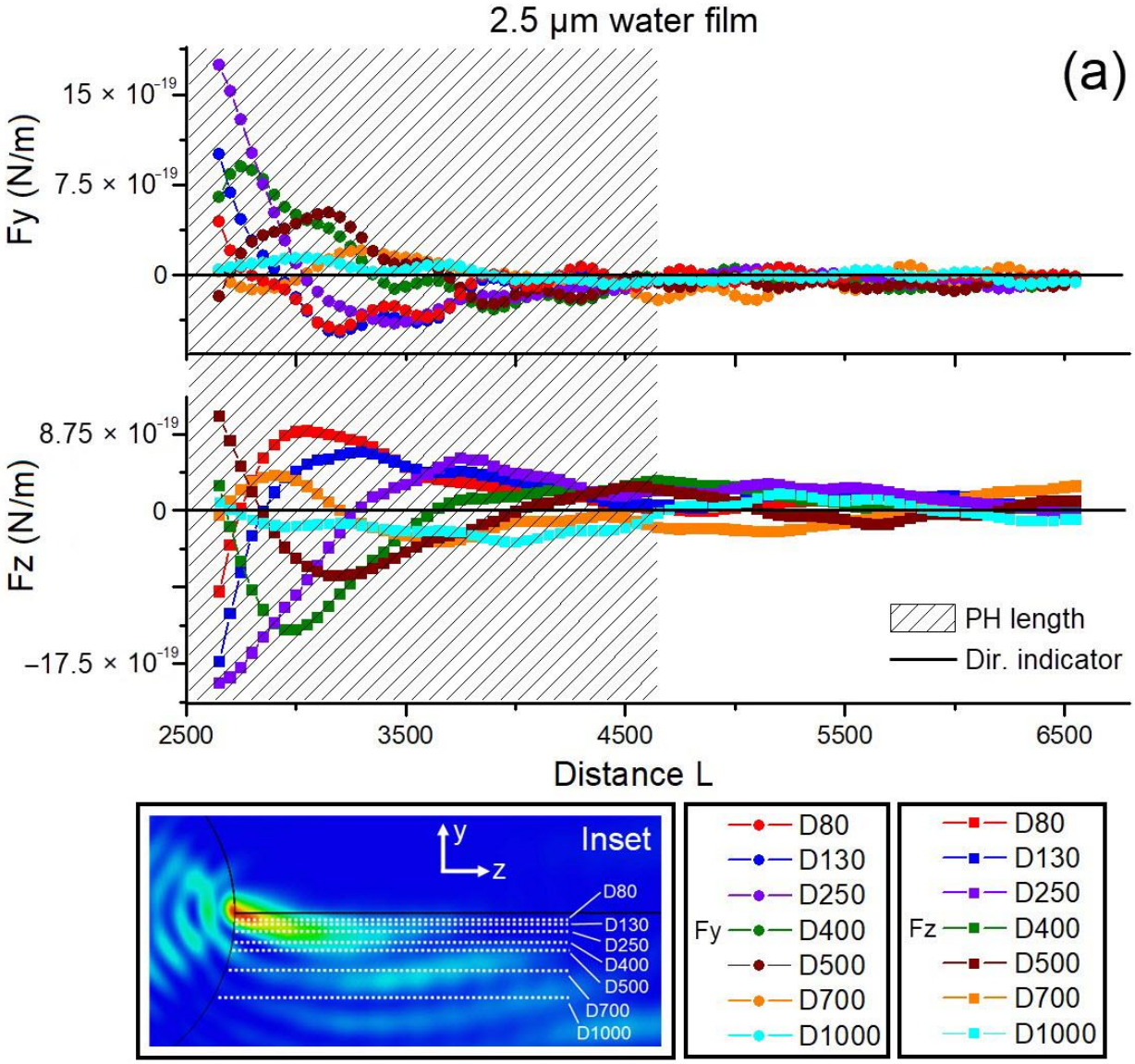

Figure 4. *Cont.*

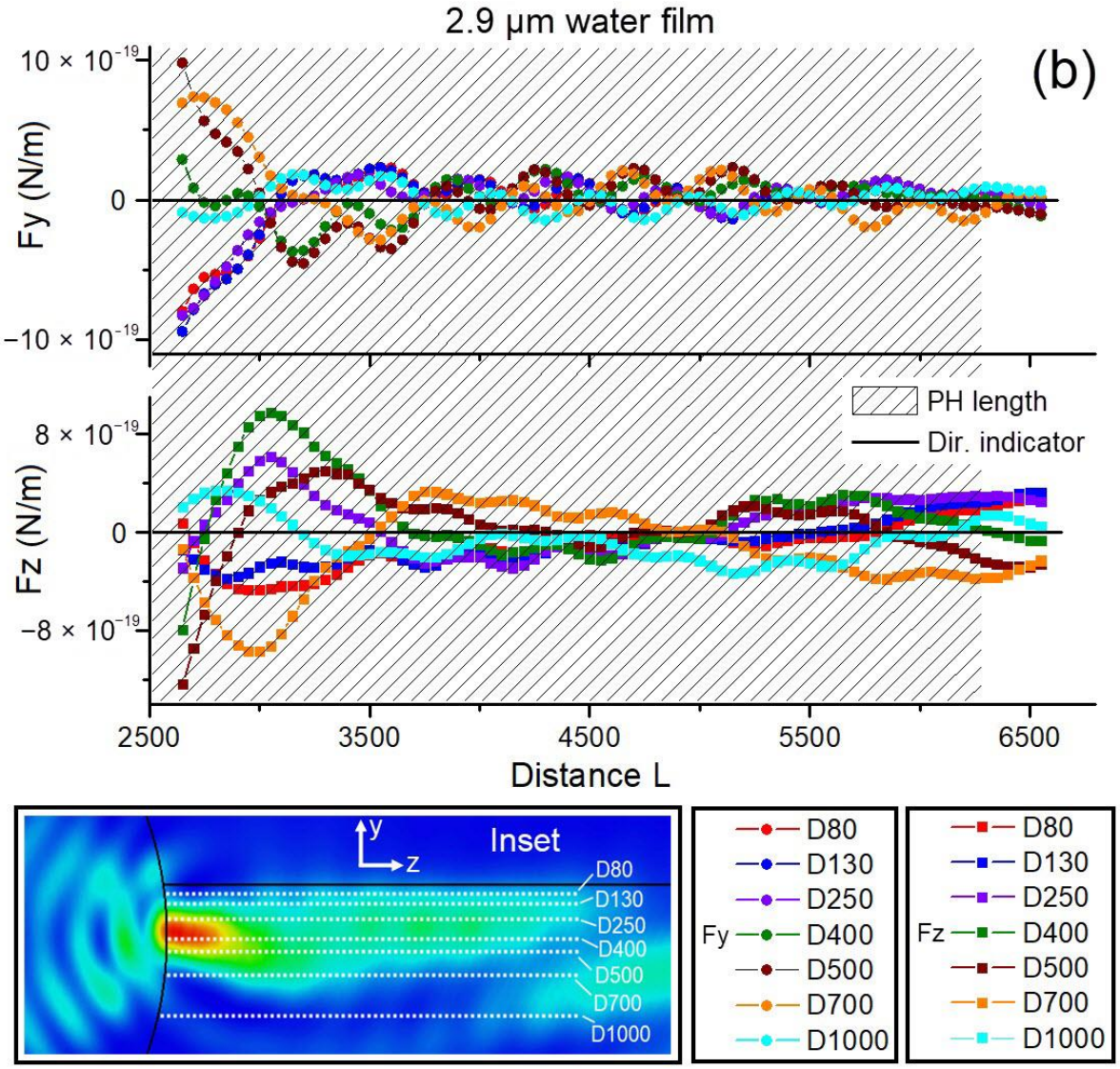

Figure 4. Transverse and axial optical force pressures—F_x and F_z loaded onto the PS particle at various depths—D and distances—L in the models with the water films of (**a**) 2.5 μm and (**b**) 2.9 μm thicknesses.

Both Figure 4a,b indicate that the magnitudes of the 2D optical pressure forces are considerably large within the length of the photonic hooks and decrease inversely with the distance L and depth D. This explains the downward slope of the curves on the left sides of the figures as L increases. In addition to the curvature and length, the distance between the photonic hook and its ALI is also an important factor for computing the optical trapping forces. In the case of a water film with a thickness of 2.5 μm, the high-intensity area of the photonic hook partially lies above the ALI, while the rest of it and the main bending part are located underneath and overlap with the ALI, as illustrated in the inset of Figure 4a. All the data points used in the calculation are actually below the high-intensity area of the photonic hook. Due to the downward propagation of the photonic hook and the level alignment of the data points, the curves with small depths exhibit fluctuations around the force direction indicator (black solid line at 0) in Figure 4a. Nonetheless, these forces generally point towards the development of the bend photonic hook in a statistical analysis.

In contrast, the photonic hook in Figure 4b is fully immersed in a 2.9 μm thick water film and has smaller bend angles as shown in Figure 3. For this reason, the optical forces are symmetric to the indicator of force direction for F_y in the first row of Figure 4b because

the data points at small and large depths are distributed on both sides of the photonic hook and the forces are directed toward it, as shown in the inset of Figure 4b. Furthermore, regular rises and falls and wavy features appear on all curves of the optical forces in the regions far from the high-intensity areas in the photonic hooks in Figure 4a,b. This could be due to the regular oscillations of the Poynting vector streamlines in those regions, as reported in Section 3.2. Moreover, the trapping effect of a photonic hook in a relatively thick water film, e.g., the instance in Figure 4b, would be more useful because of the even and balanced optical forces in the transverse y direction, as shown in Figure 4. It has been noted that the optical force pressures shown in Figure 4 are based on the incident laser with an electric field magnitude of 1 V/m, which means the larger trapping force can be loaded on the targets using an enhanced incident laser in the magnitude of the electric field. Therefore, the optical pressures measured in this study are expected to surpass the combined adhesive forces on the surface at the air–liquid interface (ALI) following the enhancement process. This includes the crucial Van der Waals force, as evidenced by a comparison to the data obtained by Kundu et al. [48] and Jia et al. [49]. However, a detailed study of this phenomenon in relation to the trapping of nanoparticles along the ALI is beyond the scope of this article and will be the subject of future research. In view of the verification of the mechanism and experimental implementation, partial immersion and an interface to generate the proposed photonic hook could be temporarily realised by the air and a solid matter, e.g., a photoresist, which is micro-machined to an appropriate thickness and with a refractive index that is similar to that of water, to avoid the influence of surface tension and other mechanical factors at the liquid surface. In fact, because of the fact that the proposed photonic hook only exists in the small area beneath the ALI, it could be used for future optical liquid-level sensors [50] and optical trapping in biomedical applications [51]. The fabrication challenges of the proposed setup would focus on the placement of the optical fibre core (micro-cylinder) and precise control of the thickness of the water film.

4. Conclusions

This study investigates a novel photonic hook initiated by and propagating along the ALI. It exists at specific depths of a liquid film that is used to partially immerse a micro-cylinder and shows a unique bending and horizontal development at the ALI. Its formation mechanism is thought to be related to the refractive index contrasts around the ALI in the shadow direction of the micro-cylinder, based on an analysis of the distributions of the electric field intensities and Poynting vector flows at various water film thicknesses. This is different from the previously reported photonic hooks, which are all caused by particle asymmetries regardless of the shape or refractive indexes at the irradiation end. The results indicate that the proposed photonic hook has unique qualities due to its attributes of the curved propagation along the ALI with a transverse dimension smaller than the diffraction limit, as well as the simulated optical forces. Optical trapping, interface cell culture, and liquid-level sensing could be the potential applications of this newfound photonic hook.

Author Contributions: Conceptualization, I.V.M. and L.Y.; Idea, I.V.M. and O.V.M.; methodology, I.V.M. and L.Y.; software, L.Y. and B.Y.; validation, I.V.M. and O.V.M.; formal analysis, I.V.M., O.V.M. and L.Y.; investigation, I.V.M., O.V.M. and L.Y.; resources, I.V.M. and L.Y.; data curation, L.Y.; writing—original draft preparation, L.Y.; writing—review and editing, I.V.M., O.V.M. and L.Y.; visualization, L.Y.; supervision, I.V.M. and O.V.M.; funding acquisition, L.Y. and Z.W. All authors have read and agreed to the published version of the manuscript.

Funding: The Royal Society International Exchanges Cost Share Scheme UK, grant numbers IEC\R2\202040 and IEC\R2\202178; the Russian Foundation for Basic Research, grant number 21-58i-10005; Leverhulme Trust (RF-2022-659).

Institutional Review Board Statement: Not applicable.

Informed Consent Statement: Not applicable.

Data Availability Statement: Data underlying the results presented in this paper are not publicly available at this time but may be obtained from the authors upon reasonable request.

Acknowledgments: All authors acknowledge the support from the Tomsk Polytechnic University Development Program.

Conflicts of Interest: The authors declare no conflict of interest.

References

1. Heifetz, A.; Kong, S.C.; Sahakian, A.V.; Taflove, A.; Backman, V. Photonic Nanojets. *J. Comput. Theor. Nanosci.* **2009**, *6*, 1979–1992. [CrossRef] [PubMed]
2. Chen, Z.; Taflove, A.; Backman, V. Photonic nanojet enhancement of backscattering of light by nanoparticles: A potential novel visible-light ultramicroscopy technique. *Opt. Express* **2004**, *12*, 1214–1220. [CrossRef] [PubMed]
3. Luk'yanchuk, B.S.; Paniagua-Domínguez, R.; Minin, I.V.; Minin, O.V.; Wang, Z. Refractive index less than two: Photonic nanojets yesterday, today and tomorrow. *Opt. Mater. Express* **2017**, *7*, 1820–1847. [CrossRef]
4. Bachynski, M.P.; Bekefi, G. Study of Optical Diffraction Images at Microwave Frequencies. *J. Opt. Soc. Am.* **1957**, *47*, 428–438. [CrossRef]
5. Stamnes, J. *Waves in Focal Regions, Chapter 10.3 Focusing with First–Order Cylindrical Aberrations*; CRC Press: New York, NY, USA, 1986.
6. Darafsheh, A. Photonic nanojets and their applications. *J. Phys. Photonics* **2021**, *3*, 022001. [CrossRef]
7. Minin, I.V.; Minin, O.V. *Diffractive Optics and Nanophotonics: Resolution below the Diffraction Limit*; Springer: Berlin, Germany, 2016.
8. Yue, L.; Minin, O.V.; Wang, Z.; Monks, J.N.; Minin, I.V. Photonic hook: A new curved light beam. *Opt. Lett.* **2018**, *43*, 771–774. [CrossRef]
9. Minin, O.V.; Minin, I.V. *The Photonic Hook: From Optics to Acoustics and Plasmonics*; Springer Nature: Berlin, Germany, 2021.
10. Dholakia, K.; Bruce, G.D. Optical hooks. *Nat. Photonics* **2019**, *13*, 229–230. [CrossRef]
11. Minin, I.V.; Minin, O.V. Recent trends in optical manipulation inspired by mesoscale photonics and diffraction optics. *J. Biomed. Photonics Eng.* **2020**, *6*, 020301. [CrossRef]
12. Gu, G.; Shao, L.; Song, J.; Qu, J.; Zheng, K.; Shen, X.; Peng, Z.; Hu, J.; Chen, X.; Chen, M.; et al. Photonic Hooks Janus Microcylinders. *Opt. Express* **2019**, *27*, 37771–37780. [CrossRef]
13. Minin, I.V.; Minin, O.V.; Liu, C.; Wei, H.; Geints, Y.; Karacevsky, A. Experimental demonstration of a tunable photonic hook by a partially illuminated dielectric microcylinder. *Opt. Lett.* **2020**, *45*, 4899–4902. [CrossRef]
14. Minin, I.V.; Minin, O.V.; Liu, Y.; Tuchin, V.V.; Liu, C. Concept of photonic hook scalpel generated by shaped fiber tip with asymmetric radiation. *J. Biophotonics* **2021**, *14*, e202000342. [CrossRef] [PubMed]
15. Chang, T.M. Chapter 1—Molecular Perspective of Gas–Liquid Interfaces: What Can Be Learned from Theoretical Simulations? In *Developments in Physical & Theoretical Chemistry, Physical Chemistry of Gas-Liquid Interfaces*; Faust, J.A., House, J.E., Eds.; Elsevier: Amsterdam, The Netherlands, 2018; pp. 1–40.
16. George, C.; Brüggemann, M.; Hayeck, N.; Tinel, L.; Donaldson, J. Chapter 14—Interfacial Photochemistry. In *Developments in Physical & Theoretical Chemistry, Physical Chemistry of Gas-Liquid Interfaces*; Faust, J.A., House, J.E., Eds.; Elsevier: Amsterdam, The Netherlands, 2018; pp. 435–457.
17. Jesacher, A.; Fürhapter, S.; Maurer, C.; Bernet, S.; Ritsch-Marte, M. Holographic optical tweezers for object manipulations at an air-liquid surface. *Opt. Express* **2006**, *14*, 6342–6352. [CrossRef]
18. Dasgupta, R.; Ahlawat, S.; Gupta, P.K. Trapping of micron-sized objects at a liquid–air interface. *J. Opt. A Pure Appl. Opt.* **2017**, *9*, S189. [CrossRef]
19. Girot, A.; Danné, N.; Würger, A.; Bickel, T.; Ren, K.F.; Loudet, J.C.; Pouligny, B. Motion of Optically Heated Spheres at the Water–Air Interface. *Langmuir* **2016**, *32*, 2687–2697. [CrossRef] [PubMed]
20. Minin, I.V.; Minin, O.V. Optical Phenomena in Mesoscale Dielectric Particles. *Photonics* **2021**, *8*, 591. [CrossRef]
21. Neuman, K.C.; Block, S.M. Optical trapping. *Rev. Sci. Instrum.* **2004**, *75*, 2787–2809. [CrossRef]
22. Xie, C.; Mace, J.; Dinno, M.A.; Li, Y.Q.; Tang, W.; Newton, R.J.; Gemperline, P.J. Identification of Single Bacterial Cells in Aqueous Solution Using Confocal Laser Tweezers Raman Spectroscopy. *Anal. Chem.* **2005**, *77*, 4390–4397. [CrossRef]
23. Fuhr, G.; Müller, T.; Schnelle, T.; Hagedorn, R.; Voigt, A.; Fiedler, S.; Arnold, W.M.; Zimmermann, U.; Wagner, B.; Heuberger, A. Radio-frequency microtools for particle and liver cell manipulation. *Die Naturwissenschaften* **1994**, *81*, 528–535. [CrossRef]
24. Casabella, S.; Scully, P.; Goddard, N.; Gardner, P. Automated analysis of single cells using Laser Tweezers Raman Spectroscopy. *Analyst* **2016**, *141*, 689–696. [CrossRef]
25. Zhang, P.; Kong, L.; Setlow, P.; Li, Y. Multiple-trap laser tweezers Raman spectroscopy for simultaneous monitoring of the biological dynamics of multiple individual cells. *Opt. Lett.* **2010**, *35*, 3321–3323. [CrossRef]
26. Zhong, M.; Wang, X.; Zhou, J.; Wang, Z.; Li, Y. Optimal beam diameter for lateral optical forces on microspheres at a water-air interface. *Chin. Opt. Lett.* **2014**, *12*, 011403. [CrossRef]
27. Liberale, C.; Minzioni, P.; Bragheri, F.; De Angelis, F.; Di Fabrizio, E.; Cristiani, I. Miniaturized all-fibre probe for three-dimensional optical trapping and manipulation. *Nat. Photon.* **2007**, *1*, 723–727. [CrossRef]
28. Xin, H.; Li, B. Fiber-based optical trapping and manipulation. *Front. Optoelectron.* **2019**, *12*, 97–110. [CrossRef]

29. Gao, B.; Zhong, H.; Yan, B.; Yue, L.; Dang, Y.; Chen, P.; Jiang, C.; Wang, Z. Combined single/dual fiber optical trapping for flexible particle manipulation. *Opt. Lasers Eng.* **2023**, *161*, 107373. [CrossRef]
30. Lou, Y.; Wu, D.; Pang, Y. Optical Trapping and Manipulation Using Optical Fibers. *Adv. Fiber Mater.* **2019**, *1*, 83–100. [CrossRef]
31. Soifer, V.A. *Diffractive Optics and Nanophotonics*; Taylor & Francis Group: Abingdon, UK, 2014.
32. Yu, J.; Xu, Y.; Lin, S.; Zhu, X.; Gbur, G.; Cai, Y. Longitudinal optical trapping and manipulating Rayleigh particles by spatial nonuniform coherence engineering. *Phys. Rev. A* **2022**, *106*, 033511. [CrossRef]
33. Brunetti, G.; Sasanelli, N.; Armenise, M.N.; Ciminelli, C. Nanoscale Optical Trapping by Means of Dielectric Bowtie. *Photonics* **2022**, *9*, 425. [CrossRef]
34. Liang, Y.; Su, Y.; Li, J.; Yang, C. Optical trapping of Rayleigh particles based on four-petal Gaussian vortex beams. *J. Opt. Soc. Am. A* **2022**, *39*, 1378–1384. [CrossRef]
35. Park, B.J.; Furst, E.M. Optical Trapping Forces for Colloids at the Oil−Water Interface. *Langmuir* **2008**, *24*, 13383–13392. [CrossRef]
36. Li, Y.; Liu, X.; Li, B. Single-cell biomagnifier for optical nanoscopes and nanotweezers. *Light Sci. Appl.* **2019**, *8*, 61. [CrossRef]
37. Blázquez-Castro, A. Optical Tweezers: Phototoxicity and Thermal Stress in Cells and Biomolecules. *Micromachines* **2019**, *10*, 507. [CrossRef] [PubMed]
38. Schott Glass Data Sheets. Available online: https://www.schott.com/shop/advanced-optics/en/Optical-Glass/N-SK4/c/glass-N-SK4 (accessed on 5 April 2023).
39. Hoang, V.T.; Stępniewski, G.; Czarnecka, K.H.; Kasztelanic, R.; Long, V.C.; Xuan, K.D.; Shao, L.; Śmietana, M.; Buczyński, R. Optical Properties of Buffers and Cell Culture Media for Optofluidic and Sensing Applications. *Appl. Sci.* **2019**, *9*, 1145. [CrossRef]
40. Haslett, C.J. *Essentials of Radio Wave Propagation*; Cambridge University Press: Cambridge, UK, 2008.
41. Cheng, D.K. *Field and Wave Electromagnetics*, 2nd ed.; Addison-Wesley: New York, NY, USA, 1989.
42. CST Studio Suite Help Document, Frequency Domain Solver Overview and Settings. Available online: https://space.mit.edu/RADIO/CST_online/cst_studio_suite_help.htm (accessed on 28 July 2023).
43. Kemp, B.A.; Grzegorczyk, T.M.; Kong, J.A. Ab initio study of the radiation pressure on dielectric and magnetic media. *Opt. Express* **2005**, *13*, 9280–9291. [CrossRef] [PubMed]
44. Zhang, X.; Qiu, J.; Li, X.; Zhao, J.; Liu, L. Complex refractive indices measurements of polymers in visible and near-infrared bands. *Appl. Opt.* **2020**, *59*, 2337–2344. [CrossRef]
45. Born, M.; Wolf, E. *Principles of Optics*; Cambridge University Press: Cambridge, UK, 1997.
46. Vettenburg, T.; Dalgarno, H.C.; Nylk, J.; Coll-Llado, C.; Ferrier, D.E.K.; Cizmar, T.; Gunn-Moore, F.J.; Dholakia, K. Light-sheet microscopy using an Airy beam. *Nat. Methods* **2014**, *11*, 541–544. [CrossRef]
47. Yue, L.; Wang, Z.; Yan, B.; Xie, Y.; Geints, Y.E.; Minin, O.V.; Minin, I.V. Near-Field Light-Bending Photonic Switch: Physics of Switching Based on Three-Dimensional Poynting Vector Analysis. *Photonics* **2022**, *9*, 154. [CrossRef]
48. Kundu, A.; Paul, S.; Banerjee, S.; Banerjee, A. Measurement of Van der Waals force using oscillating optical tweezers. *Appl. Phys. Lett.* **2019**, *115*, 123701. [CrossRef]
49. Jia, Q.; Lyu, W.; Yan, W.; Tang, W.; Lu, J.; Qiu, M. Optical manipulation: From fluid to solid domains. *Photonics Insights* **2023**, *2*, R05. [CrossRef]
50. He, R.; Teng, C.; Kumar, S.; Marques, C.; Min, R. Polymer Optical Fiber Liquid Level Sensor: A Review. *IEEE Sens. J.* **2022**, *22*, 1081–1091. [CrossRef]
51. Baker, J.; Ryan, J.E.; Badman, P.; Wang, M.D. Nanophotonic trapping: Precise manipulation and measurement of biomolecular arrays. *WIREs Nanomed. Nanobiotechnol.* **2018**, *10*, e1477. [CrossRef]